Journal of Biomedical Optics 8(1), 53–62 (January 2003)

Interplay of tumor vascular oxygenation and tumor pO_2 observed using near-infrared spectroscopy, an oxygen needle electrode, and ^{19}F MR pO_2 mapping

Jae G. Kim
University of Texas at Arlington/University of Texas Southwestern Medical Center at Dallas
Joint Graduate Program in Biomedical Engineering
Arlington, Texas 76019

Dawen Zhao
University of Texas Southwestern Medical Center at Dallas
Advanced Radiological Sciences
Department of Radiology
Dallas, Texas 75390

Yulin Song
University of Texas at Arlington/University of Texas Southwestern Medical Center at Dallas
Joint Graduate Program in Biomedical Engineering
Arlington, Texas 76019
and
University of Texas Southwestern Medical Center at Dallas
Advanced Radiological Sciences
Department of Radiology
Dallas, Texas 75390

Anca Constantinescu
Ralph P. Mason
University of Texas Southwestern Medical Center at Dallas
Advanced Radiological Sciences
Department of Radiology
Dallas, Texas 75390

Hanli Liu
University of Texas at Arlington/University of Texas Southwestern Medical Center at Dallas
Joint Graduate Program in Biomedical Engineering
Arlington, Texas 76019

Abstract. This study investigates the correlation of tumor blood oxygenation and tumor pO_2 with respect to carbogen inhalation. After having refined and validated the algorithms for calculating hemoglobin concentrations, we used near-infrared spectroscopy (NIRS) to measure changes of oxygenated hemoglobin concentration ($\Delta[HbO_2]$) and used an oxygen needle electrode and ^{19}F MRI for pO_2 measurements in tumors. The measurements were taken from Dunning prostate R3327 tumors implanted in rats, while the anesthetized rats breathed air or carbogen. The NIRS results from tumor measurements showed significant changes in tumor vascular oxygenation in response to carbogen inhalation, while the pO_2 electrode results showed an apparent heterogeneity for tumor pO_2 response to carbogen inhalation, which was also confirmed by ^{19}F MR pO_2 mapping. Furthermore, we developed algorithms to estimate hemoglobin oxygen saturation, sO_2, during gas intervention based on the measured values of $\Delta[HbO_2]$ and pO_2. The algorithms have been validated through a tissue-simulating phantom and used to estimate the values of sO_2 in the animal tumor measurement based on the NIRS and global mean pO_2 values. This study demonstrates that the NIRS technology can provide an efficient, real-time, noninvasive approach to monitoring tumor physiology and is complementary to other techniques, while it also demonstrates the need for an NIR imaging technique to study spatial heterogeneity of tumor vasculature under therapeutic interventions.
[DOI: 10.1117/1.1527049]

Keywords: frequency-domain spectroscopy; NIR spectroscopy; ^{19}F MRI; tumor vascular oxygenation; pO_2 electrode; oxygen; oximetry.

Paper 01078 received Nov. 13, 2001; revised manuscript received June 25, 2002; accepted for publication Aug. 26, 2002.

1 Introduction

It has long been known that hypoxic tumor cells are more resistant to radiation therapy than well-oxygenated tumor cells.[1] Breathing elevated oxygen (100%) or carbogen (95% O_2, 5% CO_2) has been used during therapy for an attempt to improve tumor oxygenation.[2,3] To monitor tumor tissue oxygen tension[4] and its dynamic changes under respiratory interventions, various methods are available, including fiber optic sensors,[5] oxygen electrodes,[6] and electron spin resonance.[7] MRI has the further advantage of providing dynamic maps of pO_2, which can reveal tumor heterogeneity.[8] While NIRS does not quantify pO_2, it can indicate dynamic changes in vascular oxygenation and has the advantage of being entirely noninvasive, providing real-time measurements, and being cost-effective and portable. Furthermore, it would be important to correlate the changes between tissue pO_2 and vascular oxygenation of the tumors since little is known about oxygen transfer from the tumor vasculature to tumor tissue.

The basic principle of NIRS rests on the fact that oxygenated and deoxygenated hemoglobin molecules are major chromophores in tissue in the near-infrared region (700 to 900 nm), and they exhibit distinct absorption characteristics. In principle, the concentrations of oxygenated hemoglobin $[HbO_2]$, deoxygenated hemoglobin [Hb], and oxygen saturation of hemoglobin sO_2 can be determined by measuring light absorption and scattering in tissue based on diffusion theory. However, the theory works well only for large and homogeneous media.[9,10] Accurate quantification of tumor oxygenation in our approach is currently limited to relative changes in $[HbO_2]$ and [Hb] due to considerable heterogeneity and finite size of tumors.

The goal of this study was to investigate the correlation of tumor blood oxygenation and tumor pO_2 in response to car-

Address all correspondence to Hanli Liu. Tel: 817-272-2054; Fax: 817-272-2251; E-mail: hanli@uta.edu

1083-3668/2003/$15.00 © 2003 SPIE

bogen intervention and to develop a suitable algorithm to estimate the hemoglobin oxygen saturation of the tumor under the intervention. Specifically, in Sec. 2 of this paper, we derive accurate expressions for calculating changes in $[HbO_2]$ and [Hb] to compensate for the differences in optical path length at two wavelengths and an algorithm to estimate absolute sO_2 values of the tumor during gas intervention. The algorithms are validated through tissue-simulating phantoms and used to estimate tumor sO_2 in the animal measurement using the NIRS and mean pO_2 values, as mentioned in Secs. 3 and 4. In Sec. 4, we will show that while NIRS results tended to be similar for several tumors, pO_2 electrode measurements showed considerable variation even in the same tumor type, suggesting distinct tumor heterogeneity. In Sec. 5, we discuss the need to develop an NIR imaging technique in order to study spatial heterogeneity of tumor vasculature under oxygen interventions. Finally, we conclude that the NIRS technology can provide an efficient, real-time, noninvasive approach to monitoring tumor physiology and is complementary to other techniques.

2 Theory and Algorithm Development

2.1 Algorithms to Quantify Changes in $[HbO_2]$ and [Hb]

NIR spectroscopy can be used to measure hemoglobin concentrations and oxygen saturation since light absorptions of HbO_2 and Hb are different at the wavelengths selected (758 and 785 nm). In common with our previous work,[11] we assumed that HbO_2 and Hb are the only significant absorbing materials in tumors within the selected NIR range of 700 to 900 nm. Based on Beer-Lambert's law, the absorption coefficients μ_a comprise the extinction coefficients for deoxyhemoglobin ($\varepsilon_{\mathrm{Hb}}$) and oxyhemoglobin ($\varepsilon_{\mathrm{HbO2}}$) multiplied by their respective concentrations:

$$\mu_a^{758} = 2.3\{\varepsilon_{\mathrm{Hb}}^{758}[\mathrm{Hb}] + \varepsilon_{\mathrm{HbO2}}^{758}[\mathrm{HbO_2}]\}, \tag{1}$$

$$\mu_a^{785} = 2.3\{\varepsilon_{\mathrm{Hb}}^{785}[\mathrm{Hb}] + \varepsilon_{\mathrm{HbO2}}^{785}[\mathrm{HbO_2}]\}, \tag{2}$$

where the factor of 2.3 results from the different definitions of μ_a and ε in relation to the incident and detected optical intensities. The conventional definitions for μ_a and ε are $I = I_0 \exp(-\mu_a L)$ and $I = I_0 10^{-\varepsilon CL}$, respectively, where I_0 and I are the incident and detected optical intensities in transmission measurement of a nonscattering medium, C is the concentration of hemoglobin measured in millimoles per liter, and L is the optical path length through the medium in centimeters. Therefore, we should have a relationship of $\mu_a = 2.3\,\varepsilon C$.

We have not yet completed a suitable algorithm to compute μ_a of rat tumors due to their finite size and high heterogeneity. Instead of diffusion theory, we modified Beer-Lambert's law, i.e., $\mu_a = 2.3\varepsilon C = (2.3/L)\log(I_0/I)$, to analyze the data using only amplitude values to quantify changes in $[HbO_2]$ and [Hb]. In this case, I_0 is the detected light intensity when no absorption is present. Specifically, changes in absorption coefficient of the tumor, $\Delta\mu_a$, between baseline and transient conditions under respiratory intervention can be expressed as

$$\Delta\mu_a = \mu_{aT} - \mu_{aB} = 2.3\log(A_B/A_T)/L, \tag{3}$$

where L is the optical path length and A_B and A_T are baseline and transient amplitudes of the measured optical signals, respectively.

By manipulating Eqs. (1) to (3), changes of $[HbO_2]$ and [Hb] due to an intervention can be expressed using the transmitted amplitudes of the light through the tumor as:

$$\Delta[\mathrm{HbO_2}] = -11.73^* \frac{\log(A_B/A_T)^{758}}{L^{758}} + 14.97^* \frac{\log(A_B/A_T)^{785}}{L^{785}}, \tag{4}$$

$$\Delta[\mathrm{Hb}] = 8.09^* \frac{\log(A_B/A_T)^{758}}{L^{758}} - 6.73^* \frac{\log(A_B/A_T)^{785}}{L^{785}}, \tag{5}$$

where L^{758} and L^{785} are optical path lengths between the source and detector at 758 and 785 nm, respectively. The units of $\Delta[HbO_2]$ and Δ[Hb] in Eqs. (4) and (5) are in millimolar. The constants given in the equations were computed with the extinction coefficients for oxygenated and deoxygenated hemoglobin at the two wavelengths used.[12] The constant values are slightly different from our previous report[11] due to a slight shift in wavelength (782 to 785 nm) from one laser source, but the actual differences between the values of $\Delta[HbO_2]$ and Δ[Hb] calculated from our previous report and from Eqs. (4) and (5) are little and negligible.

In principle, L^{758} and L^{785} given in Eqs. (4) and (5) are not constants, depending on both the source-detector separation and the optical properties of the measured medium. Optical path length in a scattering medium L has been expressed[13] as the source-detector separation d multiplied by a differential pathlength factor (DPF), i.e., $L = d^*DPF$. DPF values of blood-perfused tissues should be wavelength- and oxygenation-dependent, and they have been studied intensively for muscles[14] and brains[15] with approximate values of 4 to 6 and 5 to 6, respectively. Little is known about DPF for tumors although a DPF value of 2.5 has been used by others.[16] In our approach, we define two parameters, β_{HbO2} and β_{Hb}, as ratios between DPF^{758} and DPF^{785} for oxygenated blood and deoxygenated blood, respectively, as given below:

$$\beta_{\mathrm{HbO2}} = \left(\frac{DPF^{758}}{DPF^{785}}\right)_{\mathrm{HbO2}} = \left(\frac{L^{758}}{L^{785}}\right)_{\mathrm{HbO2}},$$

$$\beta_{\mathrm{Hb}} = \left(\frac{DPF^{758}}{DPF^{785}}\right)_{\mathrm{Hb}} = \left(\frac{L^{758}}{L^{785}}\right)_{\mathrm{Hb}}. \tag{6}$$

Substituting Eq. (6) into Eqs. (4) and (5) leads to

$$\Delta[\mathrm{HbO_2}] = \frac{-\frac{11.73}{\beta_{\mathrm{HbO2}}}\log\left(\frac{A_B}{A_T}\right)^{758} + 14.97\log\left(\frac{A_B}{A_T}\right)^{785}}{d \times DPF_0}, \tag{7}$$

$$\Delta[\mathrm{Hb}]=\frac{\frac{8.09}{\beta_{\mathrm{Hb}}}\log\left(\frac{A_B}{A_T}\right)^{758}-6.73\log\left(\frac{A_B}{A_T}\right)^{785}}{d\times DPF_0}, \quad (8)$$

where DPF_0 is a mean DPF at 785 nm for both oxygenated and deoxygenated states, i.e., $DPF_0=DPF^{785}_{\mathrm{HbO2}}=DPF^{785}_{\mathrm{Hb}}$, which is assumed to be the same for both $\Delta[\mathrm{HbO_2}]$ and $\Delta[\mathrm{Hb}]$. This assumption is based on the fact that the absorption difference between oxygenated and deoxygenated blood at 785 nm is much smaller than that at 758 nm. The maximal relative error caused by this assumption in tumor oxygen interventions was estimated to be less than 12%, and detailed justification and discussion were given in Ref. 11. Since our focus is on dynamic changes in tumor $[\mathrm{HbO_2}]$ under carbogen intervention, we simplify Eqs. (7) and (8) to Eqs. (9) and (10) by including DPF_0 in the unit:

$$\Delta[\mathrm{HbO_2}]=\frac{-\frac{11.73}{\beta_{\mathrm{HbO2}}}\log\left(\frac{A_B}{A_T}\right)^{758}+14.97\log\left(\frac{A_B}{A_T}\right)^{785}}{d}, \quad (9)$$

$$\Delta[\mathrm{Hb}]=\frac{\frac{8.09}{\beta_{\mathrm{Hb}}}\log\left(\frac{A_B}{A_T}\right)^{758}-6.73\log\left(\frac{A_B}{A_T}\right)^{785}}{d}, \quad (10)$$

where the units for Eqs. (9) and (10) become $\mathrm{mM/DPF_0}$.

To further quantify β_{HbO2} and β_{Hb}, we associate L to μ_a by $L=(\sqrt{3}/2)d\,(\mu_s'/\mu_a')^{1/2}$, where μ_s' is the reduced scattering coefficient, according to Sevick et al.[10] and Liu.[17] Equation (6) becomes

$$\beta_{\mathrm{HbO2}}=\left(\frac{L^{758}}{L^{785}}\right)_{\mathrm{HbO2}}=\left[\left(\frac{\mu_a^{785}}{\mu_a^{758}}\right)^{1/2}\right]_{\mathrm{HbO2}}=\left[\left(\frac{\varepsilon^{785}}{\varepsilon^{758}}\right)^{1/2}\right]_{\mathrm{HbO2}}, \quad (11)$$

$$\beta_{\mathrm{Hb}}=\left(\frac{L^{758}}{L^{785}}\right)_{\mathrm{Hb}}=\left[\left(\frac{\mu_a^{785}}{\mu_a^{758}}\right)^{1/2}\right]_{\mathrm{Hb}}=\left[\left(\frac{\varepsilon^{785}}{\varepsilon^{758}}\right)^{1/2}\right]_{\mathrm{Hb}}, \quad (12)$$

where $\mu_a=2.3\,\varepsilon C$ and μ_s' values at two wavelengths are canceled, assuming that μ_s' (758 nm)$\cong\mu_s'$ (785 nm). By calculating the hemoglobin extinction coefficients at 758 and 785 nm,[12] we obtained $\beta_{\mathrm{HbO2}}=1.103$ and $\beta_{\mathrm{Hb}}=0.9035$. Substituting these values into Eqs. (9) and (10) results in the final expressions for $\Delta[\mathrm{HbO_2}]$ and $\Delta[\mathrm{Hb}]$:

$$\Delta[\mathrm{HbO_2}]=\frac{-10.63\log\left(\frac{A_B}{A_T}\right)^{758}+14.97\log\left(\frac{A_B}{A_T}\right)^{785}}{d}, \quad (13)$$

$$\Delta[\mathrm{Hb}]=\frac{8.95\log\left(\frac{A_B}{A_T}\right)^{758}-6.73\log\left(\frac{A_B}{A_T}\right)^{785}}{d}. \quad (14)$$

$\Delta[\mathrm{Hb_{total}}]$ can also be obtained by adding Eqs. (13) and (14):

$$\Delta[\mathrm{Hb_{total}}]=\Delta[\mathrm{HbO_2}]+\Delta[\mathrm{Hb}]=\frac{-1.68\log\left(\frac{A_B}{A_T}\right)^{758}+8.24\log\left(\frac{A_B}{A_T}\right)^{785}}{d}. \quad (15)$$

Equations (13) to (15) will be used in calculating $\Delta[\mathrm{HbO_2}]$, $\Delta[\mathrm{Hb}]$, and $\Delta[\mathrm{Hb_{total}}]$ in tissue phantoms and tumors during gas interventions in this paper.

The units for $\Delta[\mathrm{HbO_2}]$, $\Delta[\mathrm{Hb}]$, and $\Delta[\mathrm{Hb_{total}}]$ in Eqs. (13) to (15) are $\mathrm{mM/DPF_0}$, which is still a variable, depending on the optical properties of the tumor at a particular wavelength. Since our study involves changes in $[\mathrm{HbO_2}]$ due to respiratory challenges, we can obtain a normalized $\Delta[\mathrm{HbO_2}]$ at its maximal value, i.e., $\Delta[\mathrm{HbO_2}]/\Delta[\mathrm{HbO_2}]_{\max}$, to eliminate the unit so as to minimize the effect of DPF on our results. Next, we will show that a normalized $\Delta[\mathrm{HbO_2}]$ has a close relationship with hemoglobin oxygen saturation $\mathrm{sO_2}$.

2.2 Relationship Among Normalized $\Delta[\mathrm{HbO_2}]$, $\mathrm{sO_2}$ and Blood $\mathrm{pO_2}$

We define $\mathrm{sO_2}$ values of the measured sample at the baseline, transient state, and maximal state, i.e., $(\mathrm{sO_2})_{\mathrm{base}}$, $(\mathrm{sO_2})_t$, and $(\mathrm{sO_2})_{\max}$, respectively:

$$(\mathrm{sO_2})_{\mathrm{base}}=\frac{[\mathrm{HbO_2}]_{\mathrm{base}}}{[\mathrm{Hb_{total}}]_{\mathrm{base}}}, \quad (16)$$

$$(\mathrm{sO_2})_t=\frac{[\mathrm{HbO_2}]_t}{[\mathrm{Hb_{total}}]_t}, \quad (17)$$

$$(\mathrm{sO_2})_{\max}=\frac{[\mathrm{HbO_2}]_{\max}}{[\mathrm{Hb_{total}}]_{\max}}, \quad (18)$$

where $[\mathrm{HbO_2}]_{\mathrm{base}}$, $[\mathrm{HbO_2}]_t$, and $[\mathrm{HbO_2}]_{\max}$ are corresponding to oxygenated hemoglobin concentrations at the respective state. Mathematically, it follows that

$$\frac{\Delta\mathrm{sO_2}}{\Delta\mathrm{sO_2}_{\max}}=\frac{(\mathrm{sO_2})_t-(\mathrm{sO_2})_{\mathrm{base}}}{(\mathrm{sO_2})_{\max}-(\mathrm{sO_2})_{\mathrm{base}}}=\frac{\left(\frac{[\mathrm{HbO_2}]_t}{[\mathrm{Hb_{total}}]_t}-\frac{[\mathrm{HbO_2}]_{\mathrm{base}}}{[\mathrm{Hb_{total}}]_{\mathrm{base}}}\right)}{\left(\frac{[\mathrm{HbO_2}]_{\max}}{[\mathrm{Hb_{total}}]_{\max}}-\frac{[\mathrm{HbO_2}]_{\mathrm{base}}}{[\mathrm{Hb_{total}}]_{\mathrm{base}}}\right)}. \quad (19)$$

During a cycle of oxygenation and deoxygenation in a blood-perfused tissue, if the total concentration of hemoglobin remains constant, we have the following condition: $[\mathrm{Hb_{total}}]_{\max}=[\mathrm{Hb_{total}}]_t=[\mathrm{Hb_{total}}]_{\mathrm{base}}$. In the case of tumors under gas intervention, total hemoglobin concentration does not always remain constant, but the changes in $[\mathrm{Hb}]_{\mathrm{total}}$ appeared relatively small in comparison to the changes in $[\mathrm{HbO_2}]$.[11,18] It is reasonable to assume that $\Delta[\mathrm{Hb_{total}}]\ll[\mathrm{Hb_{total}}]$, i.e., the condition of $[\mathrm{Hb_{total}}]_{\max}=[\mathrm{Hb_{total}}]_t=[\mathrm{Hb_{total}}]_{\mathrm{base}}$ still holds for the tumor under oxygen/carbogen interventions. Then, Eq. (19) becomes

$$\frac{\Delta sO_2}{\Delta sO_{2\,max}} = \frac{(sO_2)_t - (sO_2)_{base}}{(sO_2)_{max} - (sO_2)_{base}} = \frac{\Delta[HbO_2]}{\Delta[HbO_2]_{max}}. \quad (20)$$

To further make correlation between the normalized $\Delta[HbO_2]$ and blood pO_2, Hill's equation[19] can be combined with Eq. (20) to characterize oxygen transport in the tissue vasculature:

$$\frac{\Delta[HbO_2]}{\Delta[HbO_2]_{max}} = \frac{\frac{(pO_2^B)^n}{(P_{50}^B)^n + (pO_2^B)^n} - (sO_2)_{base}}{(sO_2)_{max} - (sO_2)_{base}} = \frac{\frac{(pO_2^B)^n}{(P_{50}^B)^n + (pO_2^B)^n} - b}{a - b}, \quad (21)$$

where pO_2^B is the oxygen partial pressure in blood, P_{50}^B is the oxygen partial pressure in blood at $sO_2 = 50\%$, n is the Hill coefficient, $a = (sO_2)_{max}$, and $b = (sO_2)_{base}$. This equation associates the normalized ΔHbO_2 to blood pO_2 in tissues. It indicates that normalized $\Delta[HbO_2]$ measured from tissues/tumors under gas interventions is associated with normalized sO_2 between $(sO_2)_{base}$ and $(sO_2)_{max}$ of the tissue/tumor, and it predicts the relationship between the normalized $\Delta[HbO_2]$ and blood pO_2 values in the tissue/tumor vasculature.

In our phantom studies, the measured pO_2 values are considered as blood pO_2 in tissue vasculature since blood is well mixed in the solution (see details in Sec. 3.4). Therefore, values of P_{50}^B, n, a, and b in Eq. (21) can be fitted to the experimental data, allowing us to determine the initial, transient, and maximal values of sO_2 of the simulating tissue due to oxygen/nitrogen interventions.

2.3 Relationship Between Normalized $\Delta[HbO_2]$ and Tissue/Tumor pO_2

In principle, blood pO_2 and tissue pO_2 are different, depending on the relative distance between a capillary vessel, oxygen consumption, and the location where pO_2 is measured.[19] It is shown that there exists a constant pressure drop between blood pO_2 and tissue pO_2 as the blood passes through a capillary vessel. Therefore, it is reasonable to assume

$$pO_2^B = \alpha \cdot pO_2^T, \quad (22)$$

where pO_2^B and pO_2^T are blood pO_2 and tissue pO_2 values, respectively, and α is a constant representing an oxygen partial pressure drop from blood pO_2 to a local tissue pO_2. Substituting Eq. (22) in Eq. (21) results in

$$\frac{\Delta[HbO_2]}{\Delta[HbO_2]_{max}} = \frac{\frac{(pO_2^T)^n}{(P_{50}^T)^n + (pO_2^T)^n} - b}{a - b}, \quad (23)$$

where P_{50}^T is the oxygen partial pressure in tissue resulting from P_{50}^B, and the meanings of n, a, and b remain the same as in Eq. (21). This equation shows how normalized $\Delta[HbO_2]$ measured from tissue under gas interventions is associated with both tissue pO_2 and normalized sO_2 between $(sO_2)_{base}$ and $(sO_2)_{max}$ in the tissue vasculature.

Ideally, when both $\Delta[HbO_2]$ and tissue pO_2 are measured at the same physical location, the maximal and initial oxygen saturations, i.e., a and b in Eq. (23), of the measured tissue vasculature can be obtained by fitting Eq. (23) to the measured data. In our tumor study, we then can estimate the maximal and initial hemoglobin oxygen saturations of the tumor by fitting the measured values of global normalized $\Delta[HbO_2]$ and global tissue pO_2, which result from adding up all local pO_2 values obtained from ^{19}F MR pO_2 mapping.

3 Materials and Methods

3.1 Tumor Model

Dunning prostate rat tumors (eight R3327-HI and four R3327-AT1)[20] were implanted in pedicles on the foreback of adult male Copenhagen rats, as described in detail previously.[21] Once the tumors reached approximately 1 cm in diameter, the rats were anesthetized with 0.2 ml ketamine hydrochloride (100 mg/mL; Aveco, Fort Dodge, IA) and maintained under general gaseous anesthesia with isoflurane in air (1.3% isoflurane at 1 dm^3/min air) through a mask placed over the mouth and nose. Tumors were shaved to improve optical contact for transmitting light. Body temperature was maintained by a warm water blanket and was monitored by a rectally inserted thermal probe connected to a digital thermometer (Digi-Sense, model 91100-50, Cole-Parmer Instrument Company, Vernon Hills, IL). A pulse oximeter (model 8600, Nonin, Inc., Plymouth, MN) was placed on the hind foot to monitor arterial oxygenation (S_aO_2). Tumor volume V (in cubic centimeters) was estimated as $V = (4\pi/3)[(L + W + H)/6]^3$, where L, W, and H are the three respective orthogonal dimensions.

In general, the source-detector fiber separation was about 1 to 1.5 cm in transmittance geometry, and thus the maximal tumor volume interrogated by NIR light can be estimated as follows. By the diffusion approximation, the optical penetration depth from the central line between the source and detector is about one half of the separation (source-detector separation $= d$). The total tumor volume interrogated by NIR light can be estimated as the spherical volume with a radius of one half of d, i.e., $(\pi/6)d^3$. In this way, the estimated tumor volume interrogated by NIR light is in the range of 0.5 to 2.0 cm^3, depending on the actual source-detector separation.

3.2 NIRS and pO_2 Needle Electrode Measurements

Figure 1 shows the schematic setup for animal experiments using both NIRS and a pO_2 needle electrode. A needle type oxygen electrode was placed in the tumor, and the reference electrode was placed rectally. The electrodes were connected to a picoammeter (Chemical Microsensor, Diamond Electro-Tech Inc., Ann Arbor, MI) and polarized at -0.75 V. Linear two-point calibrations were performed with air (21% O_2) and pure nitrogen (0% O_2) saturated saline buffer solutions before the electrode was inserted into the tumor, and we estimated an instrumental precision of 2 to 3 mm Hg. Measurement points of pO_2 were manually recorded, while the NIRS data were acquired automatically. Measurements of pO_2 and NIRS were initiated, while the rats breathed air for ~10 min to demonstrate a stable baseline. The inhaled gas was then switched to carbogen for 15 min and switched back to air.

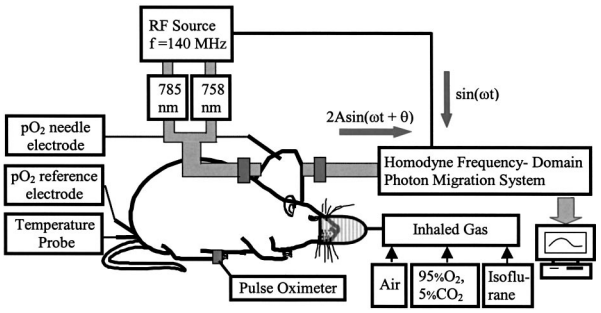

Fig. 1 Schematic experimental setup of one-channel, near-infrared, frequency-domain IQ instrument for tumor investigation *in vivo*. The 5-mm-diameter fiber bundles deliver the laser light, comprising two wavelengths (758 and 785 nm), and detect the laser light transmitted through the implanted tumor. The pO_2 needle electrode measures tumor tissue pO_2.

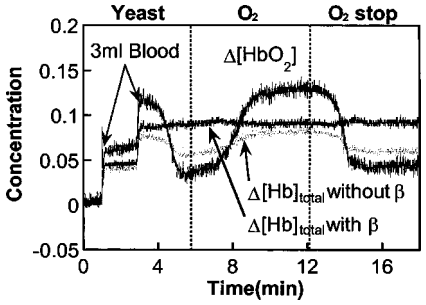

Fig. 2 Simultaneous dynamic changes of $\Delta[HbO_2]$, $\Delta[Hb]$, and $\Delta[Hb]_{total}$ in the phantom solution measured using NIRS. The gray solid curve is for $\Delta[Hb]_{total}$ without using β_{HbO_2} and β_{Hb} values. Oxygen consumption by yeast produced deoxygenated blood and blowing oxygen restored oxygenation. During the oxy- and deoxygenation process, $\Delta[Hb]_{total}$ is supposed to be a constant. However, as we can see here, $\Delta[Hb]_{total}$ calculated without β_{HbO2} and β_{Hb} values shows the fluctuation during the oxy- and deoxygenation while $\Delta[Hb]_{total}$ calculated using β_{HbO2} and β_{Hb} values shows the veracity of these modified algorithms.

Our NIR system as shown in Figure 1 (Refs. 11 and 22) is a homodyne frequency-domain photon migration system (NIM, Inc., Philadelphia, PA) and uses commercially available in-phase and quadrature (IQ) demodulator chips to demodulate the detected, amplitude-modulated optical signal.

3.3 Experimental Validation for β_{HbO2} and β_{Hb} Values

In order to validate β_{HbO2} and β_{Hb} values, we conducted phantom calibration measurements. We used 2 l of 0.01 M phosphate buffered saline (P-3813, Sigma, St Louis, MO) and 1% Intralipid (Intralipid® 20%, Baxter Healthcare Corp., Deerfield, IL) with pH = 7.4 at 25 °C. To deoxygenate the solution, 14 g of baking yeast was dissolved in the phantom solution, and pure oxygen gas was used to oxygenate the solution. After the yeast was well mixed in the solution, 3 ml of human blood was added twice. When the blood was fully deoxygenated, pure oxygen was introduced in the solution to oxygenate the blood. After the blood was fully oxygenated, oxygen blowing was stopped in order to deoxygenate the solution with yeast again.

Equations (4) and (5) were applied to the raw amplitude data to calculate $\Delta[HbO_2]$ and $\Delta[Hb]$. Large unexpected and erroneous fluctuation of $\Delta[Hb_{total}]$ ($=\Delta[HbO_2]+\Delta[Hb]$) were seen during the oxygenation and deoxygenation cycles (Figure 2). However, when we applied Eqs. (13) to (15) to calculate $\Delta[HbO_2]$, $\Delta[Hb]$, and $\Delta[Hb_{total}]$, $\Delta[Hb_{total}]$ remained constant during the oxygenation and deoxygenation cycles as expected. This demonstrates that the values of $\beta_{HbO2}=1.103$ and $\beta_{Hb}=0.9035$ are correct and necessary to compensate the differences in DPFs caused by the two different wavelengths.

3.4 Tissue Phantom Solution Model

In order to study the relationship between pO_2 and $\Delta[HbO_2]$ in regular tissues, we conducted a tissue-simulating phantom study by using the liquid solution similar to that mentioned above. In normal tissues, there are several steps of oxygen transport from the blood to tissue cells.[23] In the tissue-simulating phantom, blowing oxygen gas represents oxygenation process of blood in the lungs, and blowing nitrogen gas simulates deoxygenation process of blood in the tissues. The differences between the tissue-simulating phantom and real tissues are that there is no capillary membrane in the phantom, and that the phantom is more homogeneous than real tissues. Capillary membranes have high permeability of oxygen, so oxygen transport from blood to tissues crossing the capillary membranes occurs straightforwardly. Furthermore, normal tissues are well vascularized, and the NIR techniques are more sensitive toward measuring small vessels and vascular bed of the tissue.[24] Therefore, vasculature of normal tissues has been simulated by a turbid solution mixed with blood as a simplified laboratory model in NIRS measurements for oxygen transport from blood to normal tissues.[10,18,22]

The experimental setup shown in Figure 3 was made to simulate tumor oxygenation/deoxygenation. Oxygen needle electrodes, a pH electrode, and a thermocouple probe (model 2001, Sentron, Inc., Gig Harbor, WA) were placed in the solution, and the gas tube for delivery of N_2 or air was placed opposite the NIRS probes to minimize any liquid movement effects. Source and detector probes for the NIRS were placed in reflection geometry with a direct separation of 3 cm. The

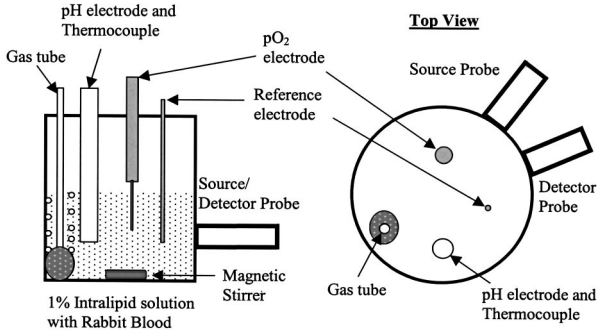

Fig. 3 Experimental setup for phantom study using 1% Intralipid in saline buffer. NIRS probes were placed in reflectance mode, while the gas bubbler was placed opposite to minimize liquid movement effects. After adding 2 ml of rabbit blood to a 200 ml solution, nitrogen gas and air were introduced to deoxygenate and oxygenate the solution, respectively.

solution was stirred constantly to maintain homogeneity by a magnetic stirrer at ~37 °C. Fresh whole rabbit blood (2 mL) was added to the 200 mL solution before baseline measurement. Nitrogen gas and air were used to deoxygenate and oxygenate the solution, respectively.

3.5 MRI Instrumentation and Procedure

To support the findings obtained from the pO_2 electrode measurements and NIRS, we conducted MRI experiments using an Omega CSI 4.7 T 40 cm system with actively shielded gradients. A homebuilt tunable $^1H/^{19}F$ single turn solenoid coil was placed around the tumor. 45 μL hexafluorobenzene (HFB; Lancaster, Gainesville, FL) was administered directly into the tumor using a Hamilton syringe (Reno, NV) with a custom-made fine sharp (32 gauge) needle and HFB was deliberated dispersal along several tracks to interrogate both central and peripheral tumor regions, as described in detail previously.[5] HFB is ideal for imaging pO_2 because it has a single resonance and its relaxation rate varies linearly with oxygen concentration. ^1H images were acquired for anatomical reference using a traditional 3-D spin-echo pulse sequence. Conventional ^{19}F MR images were taken to show the 3-D distribution of the HFB in the tumor. ^{19}F MR images were directly overlaid over ^1H images to show the position of the HFB in that slice.

Tumor oxygenation was assessed using fluorocarbon relaxometry using echo planar imaging for dynamic oxygen mapping (FREDOM) based on ^{19}F pulse burst saturation recovery (PBSR) echo planar imaging (EPI) of HFB.[25] The PBSR preparation pulse sequence consists of a series of 20 nonspatially selective saturating 90 deg pulses with 20 ms spacing to saturate the ^{19}F nuclei. Following a variable delay time τ, a single spin-echo EPI sequence with blipped phase encoding was applied.[26] Fourteen 32×32 PBSR-EPI images, with τ ranging from 200 ms to 90 sec and a field of view (FOV) of 40×40 mm, were acquired in 8 min using the alternated relaxation delays with variable acquisitions to reduce clearance effects (ARDVARC) acquisition protocol.[25] An $R1(=1/T1)$ map was obtained by fitting the signal intensity of each voxel of the 14 images to a three-parameter relaxation model by the Levenberg-Marquardt least-squares algorithm:

$$y_n(i,j)=A(i,j)\cdot[1-(1+W)\exp(-R1(i,j)\cdot\tau_n)] \tag{24}$$

$$(n=1,2,\cdots\cdots,14)$$

$$(i,j=1,2,\cdots\cdots,32),$$

where $y_n(i,j)$ is the measured signal intensity corresponding to delay time τ_n (the n'th images) for voxel (i, j), $A(i,j)$ is the fully relaxed signal intensity amplitude of voxel (i, j), W is a dimensionless scaling factor allowing for imperfect signal conversion, $R1(i,j)$ is the relaxation rate of voxel (i, j) in units of sec^{-1}, and A, W, and $R1$ are the three fit parameters for each of the 32×32 voxels. Finally, the pO_2 maps were generated by applying the calibration curve, pO_2 (mm Hg) $=[R1(s^{-1})-0.0835]/0.001876$ at 37 °C, to the $R1$ maps.[25]

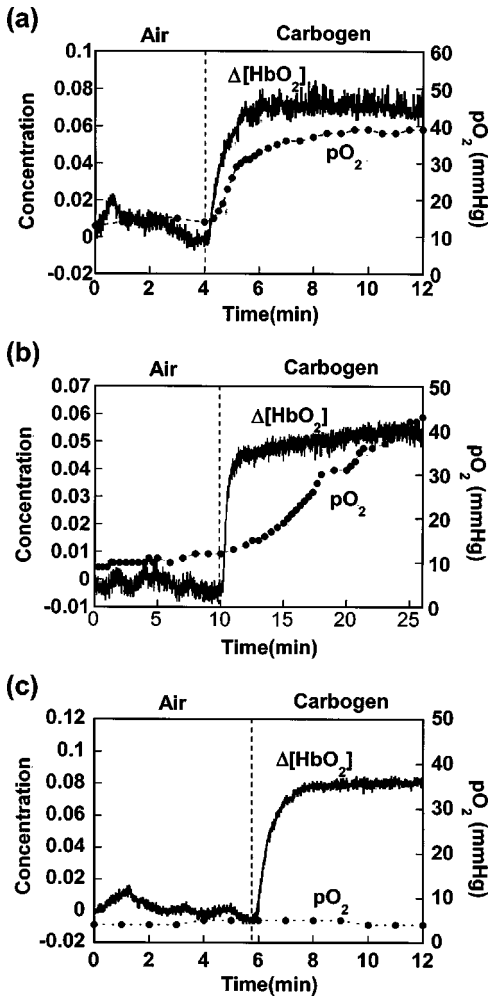

Fig. 4 Simultaneous dynamic changes of $\Delta[HbO_2]$ and pO_2 in R3327-HI rat prostate tumors using NIRS and pO_2 needle electrode. (a) A small tumor (1.5 cm^3) showed a rapid pO_2 response (case 1), whereas (b) a bigger tumor (3.1 cm^3) showed a slower pO_2 response (case 2). (c) In a third tumor (1.6 cm^3) where regional baseline pO_2 was <5 mm Hg, there was no pO_2 response (case 3). The unit of $\Delta[HbO_2]$ is mM/DPF, where DPF is equal to the optical path length divided by the source-detector separation. Dotted vertical line marks the time when the gas was changed.

4 Results

4.1 Tumor Study Results

We have measured relative changes of $[HbO_2]$, [Hb], $[Hb_{total}]$, and tumor tissue pO_2 (electrode) from eight Dunning prostate R3327-HI tumors, and Figure 4 shows three representative data sets. Figure 4(a) shows the temporal profiles of $\Delta[HbO_2]$ and pO_2 in a small Dunning prostate R3327-HI tumor (1.5 cm^3) measured simultaneously with NIRS and the pO_2 needle electrode during respiratory challenge. After a switch from air to carbogen, $\Delta[HbO_2]$ increased rapidly, along with tumor tissue pO_2. Figure 4(b) was obtained from a large tumor (3.1 cm^3): the electrode readings showed a slower pO_2 response, whereas the NIRS response was biphasic, which has been a commonly observed dynamic feature.[11] In a third tumor (1.6 cm^3), NIRS behaved as before, but pO_2 did not change [Figure 4(c)].

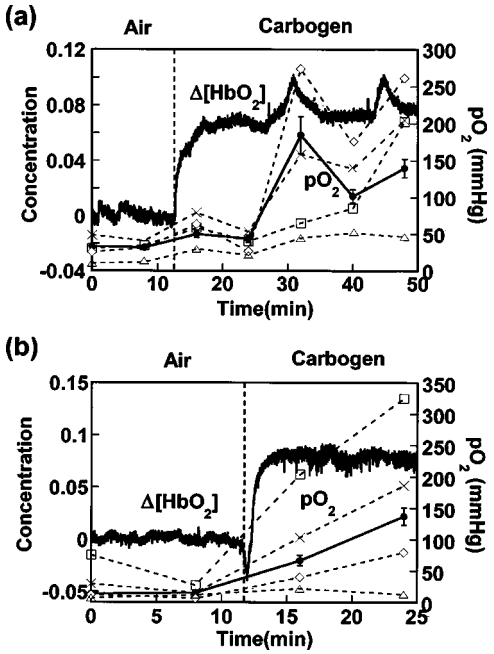

Fig. 5 Dynamic changes of $\Delta[HbO_2]$ and pO_2 in two R3327-AT1 rat prostate tumors measured sequentially using NIRS and ^{19}F MR pO_2 mapping. The solid curves represent $\Delta[HbO_2]$, and the solid lines with solid circles represent mean $pO_2 \pm$ SE (standard error) of 21 (a) and 45 (b) voxels of the respective tumor. Dashed lines with open symbols are 4 representative voxels for each case. After a gas switched from air to carbogen, the mean pO_2 values of both tumors increased, but individual voxels showed quite different responses, indicating high heterogeneity in the tumors. The tumor sizes were 3.2 cm^3 and 2.7 cm^3 for (a) and (b), respectively.

In four tumors from a separate subline (Dunning prostate R3327-AT1), NIRS and ^{19}F MRI were taken sequentially with carbogen challenge, and two representative data sets are shown in Figure 5. NIRS response showed vascular oxygenation changes as before, and FREDOM revealed the distinct heterogeneity of the tumor tissue response. Initial pO_2 was in the range of 1 to 75 mm Hg, and carbogen challenge produced pO_2 values in the range of 6 to 350 mm Hg. Representative voxels are shown in each figure by dashed lines with open symbols. In addition, mean pO_2 values were calculated by averaging all available pO_2 readings over 21 and 45 voxels for the two respective tumors. We usually obtain pO_2 temporal profiles from individual voxels among 200 to 400 voxels in a tumor during the entire intervention period. The pO_2 readings presented here were picked to show heterogeneity of the tumor. In Figure 5(a), the closest distance between the two voxels is 1.25 mm (between ◇ and □), and the furthest distance is 7.6 mm (between × and △). In Figure 5(b), the closest distance is 3.6 mm (between × and △) and the furthest distance is 16 mm (between × and □). These indeed showed that tumor pO_2 responses to carbogen intervention could be quite different at different locations. Notice that Figure 5(a) showed spikes of $\Delta[HbO_2]$ during the measurement. We expect this to be caused by sudden changes in rat respiratory circulation or motion, rather than resulting from simple instrumental noise. It is also seen that mean pO_2 values have displayed a consistent increase when $\Delta[HbO_2]$ showed spikes, suggesting that such spikes may result from changes in rat physiological conditions.

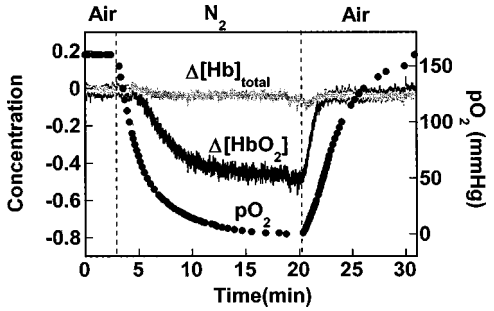

Fig. 6 Simultaneous dynamic changes of $\Delta[HbO_2]$, $\Delta[Hb]_{total}$, and pO_2 in the phantom solution measured using NIRS and pO_2 needle electrode. The dark solid curve is for $\Delta[HbO_2]$, the lighter solid line is for $\Delta[Hb]_{total}$, and the solid circles show pO_2 values in the phantom solution. After ~3 min baseline, the bubbling gas was changed from air to nitrogen to deoxygenate the solution and then switched back to air to reoxygenate the solution. The unit of $\Delta[HbO_2]$ is mM/DPF.

4.2 Tissue Phantom Study Results

Figure 6 shows a temporal profile for $\Delta[HbO_2]$ and pO_2 measured from the tissue phantom during a cycle of gas change from air to nitrogen and back. The first three minutes were measured as a baseline after adding 2 ml blood. Bubbling nitrogen deoxygenated the solution and caused the pO_2 values to fall; $\Delta[HbO_2]$ declined accordingly with a small time lag. After the bubbling gas was switched from nitrogen to air, both $\Delta[HbO_2]$ and pO_2 started to increase simultaneously, but the recovery time of $\Delta[HbO_2]$ to the baseline was faster than that of pO_2. The small time lag between the changes of $\Delta[HbO_2]$ and pO_2 is probably due to the allosteric interactions between hemoglobin and oxygen molecules. According to the hemoglobin oxygen-dissociation curve,[19,27] oxyhemoglobin starts to lose oxygen significantly when pO_2 falls below 70 mm Hg at standard conditions (pH = 7.4, pCO_2 = 40 mm Hg, and temperature = 37 °C). The same principle can explain why $\Delta[HbO_2]$ has a faster recovery than that of pO_2. Figure 6 shows that $\Delta[HbO_2]$ is already saturated when pO_2 is at 50 mm Hg, while the solution was still being oxygenated. This may be due to low pCO_2 in the solution where this can shift the oxyhemoglobin dissociation curve to the left, causing oxyhemoglobin to be saturated at lower pO_2. Importantly, $\Delta[Hb]_{total}$ remained unchanged, as expected, during a cycle of deoxygenation and oxygenation.

4.3 Correlation between pO_2 and Normalized $\Delta[HbO_2]$

For Tissue Phantoms. Figure 7(a) replots the data given in Figure 6, showing the relationship between normalized $\Delta[HbO_2]$ and pO_2 measured from the tissue phantom during the oxygenation (air blowing) period after the nitrogen blowing. Open circles are the measured data, and the solid line is the fitted curve using Eq. (23). The error bars for the data were not shown here since they are smaller than the symbols of the data points. For the curve fitting procedure, we used a nonlinear curve-fitting routine provided through KaleidaGraph (Synergy software, Reading, PA). The fitted parameters

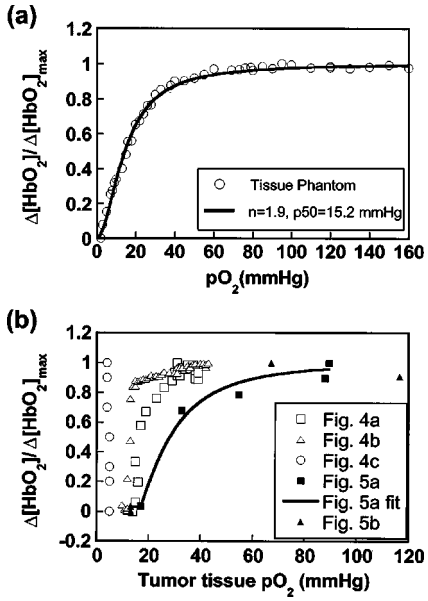

Fig. 7 Changes of tissue pO_2 with normalized changes of oxygenated hemoglobin (a) in the phantom solution using the NIRS and pO_2 needle electrode and (b) in tumors measured with NIRS, pO_2 needle electrode, and ^{19}F MR pO_2 mapping. In (a), the open circles are measured data and the solid line is the fitted curve using Eq. (21). This shows that Eq. (21) works well in a homogeneous system. In (b), all the tumor data are shown indicating that tumors are highly heterogeneous for pO_2 response to carbogen inhalation. Open symbols show local pO_2 changes (from Figure 4) and solid symbols show the mean pO_2 changes (from Figure 5) during gas intervention. To estimate global sO_2 in tumors during respiratory challenges, we applied Eq. (23) to Figure 5(a), indicating sO_2 changes during carbogen inhalation when compared via tumor pO_2.

are $n=1.9$, $P_{50}=15.2$ mm Hg, $[sO_2]_{base}=0\%$, and $[sO_2]_{max}=99\%$ with $R=0.997$ and minimized chi-square. The fitted values of $[sO_2]_{base}$ and $[sO_2]_{max}$ are in good agreement with the expected values, since the corresponding pO_2 values are 0 and 160 mm Hg, respectively. This agreement validates Eq. (23) and further indicates that we can measure approximate sO_2 values during the gas interventions in a homogeneous system by fitting the experimental data using Eq. (23) even though we do not measure absolute $[HbO_2]$. The Hill coefficient (n) and pO_2 value at 50% of sO_2 (P_{50}) are smaller than the values from a standard oxyhemoglobin saturation curve, probably due to the shift of the oxyhemoglobin dissociation curve.

For Tumor Study. Figure 7(b) replots the data given in Figures 4 and 5, showing a direct relationship between the normalized $\Delta[HbO_2]$ and tissue pO_2 in the tumors. NIRS results tended to be similar for several tumors, and pO_2 electrode measurements showed considerable variation even in the same tumor type, suggesting distinct tumor heterogeneity. This was substantiated by the ^{19}F MR pO_2 mappings (Figure 5): indeed, in some cases, pO_2 values did not change with respiratory challenge, especially when baseline pO_2 values were lower than 10 mm Hg.

Equation (23) can be used to estimate values of $[sO_2]_{base}$ and $[sO_2]_{max}$ for the tissue-simulating phantom (a homogeneous system). However, the relationship fails for heterogeneous systems such as tumors. The NIRS measurements interrogate a large volume of tumor tissue, giving a global value of normalized $\Delta[HbO_2]$, whereas the pO_2 readings are local near the tip of the needle electrode. However, to estimate mean values of $[sO_2]_{base}$ and $[sO_2]_{max}$, it is reasonable to compare the global normalized $\Delta[HbO_2]$ with global tissue pO_2, which can be obtained by summing up all local pO_2 readings at different pixels measured from the ^{19}F MRI mapping, as done in Sec. 4.1 and shown by solid lines in Figure 5. The data shown in Figure 7(b) with solid symbols are the global mean pO_2 values calculated from the corresponding MRI data. The solid fitting curve shown in Figure 7(a) is obtained from the mean pO_2 data given in Figure 5(a). In this case, the fitting parameters are P_{50}, $[sO_2]_{base}$, and $[sO_2]_{max}$ with a fixed Hill coefficient n to be the same as that under standard conditions. The best fitting curve of Eq. (23) is shown in Figure 7(b), having $P_{50}=20.6\pm4.1$ mm Hg, $[sO_2]_{base}=37\pm13\%$, and $[sO_2]_{max}=100\%$ with $R=0.985$ and goodness-of-fit $\chi^2=0.031$. Estimated errors for P_{50} and $[sO_2]_{base}$ are not insignificant and a better fit could be found by measuring pO_2 with better temporal resolution.

5 Discussion and Conclusion

Tumor oxygenation involves a complex interplay of multiple compartments and parameters: blood flow, blood volume, blood vessel structure, and oxygen consumption. NIRS provides a global noninvasive estimate of average vascular oxygenation encompassing arterial, venous, and capillary compartments. In agreement with our previous observations,[11] the $\Delta[HbO_2]$ response is often biphasic, which we believe represents rapid elevation of arterial oxygenation, followed by more sluggish capillary components.

Comparison with simultaneous electrode measurements indeed revealed that tumors are heterogeneous. Like NIRS measurements, pO_2 electrodes provide rapid assessment of pO_2 facilitating real-time observation of dynamic changes. In Figure 4(a), pO_2 starts at a baseline value ~15 mm Hg and increases rapidly in response to respiratory challenge with carbogen. Indeed, the rate approaches that of the vascular compartments. In a second tumor [Figure 4(b)], where the interrogated location showed a slightly lower pO_2, the tissue response was more sluggish. For a third HI tumor, local baseline pO_2 was found to be <5 mm Hg, and this did not change with carbogen inhalation despite the response observed by NIRS. This suggests a danger of comparing a global vascular measurement with regional tumor pO_2, since tumors are known to be highly heterogeneous. This also demonstrates an essential need for NIR imaging of tumors to provide regional tumor vascular oxygenation details.

FREDOM measurements in Figure 5 revealed the heterogeneity in baseline oxygenation within individual tumors of this second tumor subline as also reported previously.[25] Baseline pO_2 ranged from 1 to 75 mm Hg, and response to carbogen was variable in terms of rate and extent, as also seen for the HI subline using electrodes (Figure 4). As with the electrodes, the better oxygenated tumor regions showed a faster and greater response to carbogen inhalation. The oxygen electrode measurements in Figure 4 showed a maximum pO_2 of around 45 mm Hg, though we have observed values as high as 95 mm Hg using oxygen needle electrode. Observations using

the fluorescence-based OxyLite™ fiber-optic devices for measuring HI tumor reached the maximum detectable pO_2 of 100 mm Hg during carbogen inhalation.[5] FREDOM has shown values of less than 5 mm Hg and greater than 160 mm Hg under air breathing conditions, and reaching 350 mm Hg in HI tumors while breathing carbogen.[5] Each method indicates that tumors are highly heterogeneous, but it has been shown that there can be a positive linear relationship between baseline pO_2 and maximum pO_2 during carbogen inhalation in the Dunning prostate AT1 tumor line.[8]

The phantom measurements indicate and validate the reliability of the NIRS technique and also prove that normalized $\Delta[HbO_2]$ is closely related to the normalized hemoglobin-oxygen dissociation curve. The phantom data confirmed that we can obtain absolute sO_2 values in a homogeneous system by measuring both $\Delta[HbO_2]$ and pO_2. We could estimate mean sO_2 values of the tumor under intervention using global $\Delta[HbO_2]$ and averaged pO_2 readings, and the fitting errors are expected to be improved by having more data points. Measuring regional tumor vascular oxygenation by NIR imaging of tumors should allow us to correlate local $\Delta[HbO_2]$ and pO_2 and to understand the oxygen transport process from tumor vasculature to tumor tissue, and this is the direction of our future work.

Both NIRS and electrodes offer essentially real-time measurement of changes in oxygenation, which can be rapid (Figure 4). Indeed, the inflow kinetics of vascular O_2 detected by NIRS are similar to those previously reported in the HI tumor line following a bolus of the paramagnetic contrast agents Gd-DTPA.[28] FREDOM has lower temporal resolution, but reveals the tumor heterogeneity and differential response of regions exhibiting diverse baseline pO_2. The results here correspond closely with more extensive observation.[5,8,25] While FREDOM currently requires 6.5 min per pO_2 map, we have previously demonstrated an alternative data acquisition protocol achieving 1 s time resolution in a perfused heart, albeit providing less precision in measurements and only a global determination.[29] Such an approach could allow us to measure global $\Delta[HbO_2]$ and global pO_2 simultaneously with a high temporal resolution, understand the relationship between global $\Delta[HbO_2]$ and global pO_2, and obtain absolute values of sO_2 of the tumors as tumors grow.

In conclusion, we have refined the algorithms for calculating [Hb], $[HbO_2]$, and $[Hb_{total}]$ and measured relative $[HbO_2]$ changes in tumor vasculature and tumor tissue pO_2 under carbogen intervention using NIRS and a needle type pO_2 electrode. The pO_2 data were also supported by the ^{19}F MR pO_2 mapping. We have also developed an algorithm to estimate sO_2 values in the tumor during respiratory interventions. The NIRS data showed significant changes in vascular oxygenation accompanying respiratory interventions, and changes in tumor vascular oxygenation preceded tumor tissue pO_2. Oxygen electrode measurements and ^{19}F MR pO_2 mapping results proved that tumors are highly heterogeneous. The phantom data confirmed that normalized $[HbO_2]$ data together with pO_2 measurements can be used to estimate absolute sO_2 values in a homogeneous system. For a highly heterogeneous medium, such as tumors, local comparison between the $[HbO_2]$ and pO_2 value is desired and required in order to reveal the process of oxygen delivery from the tumor vascular bed to the tumor tissues. Therefore, this study not only demonstrates that the NIRS technology can provide an efficient, real-time, noninvasive approach to monitoring tumor physiology and is complementary to other techniques, but also emphasizes the need to develop an imaging technique to study spatial heterogeneity of tumor vasculature under oxygen or other therapeutic interventions.

Acknowledgments

This work was supported in part by the Department of Defense Breast Cancer Initiative grant BC990287 (HL) and NIH RO1 CA79515 (RPM). NMR experiments were conducted at the Mary Nell & and Ralph B. Rogers MR Center, an NIH BRTP Facility no. 5-P41-RR02584. We are grateful to Dr. Britton Chance from the University of Pennsylvania for assistance with tissue phantom study and to Dr. Peter Peschke for providing the original tumor cells.

References

1. L. Gray, A. Conger, M. Ebert, S. Hornsey, and O. Scott, ''The concentration of oxygen dissolved in tissues at time of irradiation as a factor in radio-therapy,'' *Br. J. Radiol.* **26**, 638–648 (1953).
2. J. H. Kaanders, L. A. Pop, H. A. Marres, J. Liefers, F. J. van den Hoogen, W. A. van Daal, and A. J. van der Kogel, ''Accelerated radiotherapy with carbogen and nicotinamide (ARCON) for laryngeal cancer,'' *Radiother. Oncol.* **48**, 115–122 (1998).
3. J. Overgaard and M. R. Horsman, ''Modification of hypoxia-induced radioresistance in tumors by the use of oxygen and sensitizers,'' *Semin. Radiat. Oncol.* **6**, 10–21 (1996).
4. H. B. Stone, J. M. Brown, and T. Phillips, ''Oxygen in human tumors: correlations between methods of measurement and response to therapy,'' *Radiat. Res.* **136**, 422–434 (1993).
5. D. Zhao, A. Constantinescu, E. W. Hahn, and R. P. Mason, ''Tumor oxygenation dynamics with respect to growth and respiratory challenge: investigation of the Dunning prostate R3327-HI tumor,'' *Radiat. Res.* **156**(5), 510–520 (2001).
6. D. Cater and I. Silver, ''Quantitative measurements of oxygen tension in normal tissues and in the tumors of patients before and after radiotherapy,'' *Acta Radiol. (1921-1962)* **53**, 233–256 (1960).
7. J. A. O'Hara, F. Goda, E. Demidenko, and H. M. Swartz, ''Effect on regrowth delay in a murine tumor of scheduling split-dose irradiation based on direct pO_2 measurements by electron paramagnetic resonance oximetry,'' *Radiat. Res.* **150**, 549–556 (1998).
8. R. P. Mason, A. Constantinescu, S. Hunjan, D. Le, E. W. Hahn, P. P. Antich, C. Blum, and P. Peschke, ''Regional tumor oxygenation and measurement of dynamic changes,'' *Radiat. Res.* **152**, 239–249 (1999).
9. M. S. Patterson, B. Chance, and B. C. Wilson, ''Time resolved reflectance and transmittance for the non-invasive measurement of tissue optical properties,'' *Appl. Opt.* **28**, 2331–2336 (1986).
10. E. M. Sevick, B. Chance, J. Leigh, S. Nokia, and M. Maris, ''Quantitation of time- and frequency-resolved optical spectra for the determination of tissue oxygenation,'' *Anal. Biochem.* **195**, 330–351 (1991).
11. H. Liu, Y. Song, K. L. Worden, X. Jiang, A. Constantinescu, and R. P. Mason, ''Noninvasive investigation of blood oxygenation dynamics of tumors by near-infrared spectroscopy,'' *Appl. Opt.* **39**, 5231–5243 (2000).
12. W. G. Zijlstra, A. Buursma, and W. P. Meeuwsen-van der Roest, ''Absorption spectra of human fetal and adult oxyhemoglobin, deoxyhemoglobin, carboxyhemoglobin, and methemoglobin,'' *Clin. Chem.* **37**, 1633–1638 (1991).
13. D. T. Delpy, M. Cope, P. van der Zee, S. Arridge, S. Wray, and J. Wyatt, ''Estimation of optical pathlength through tissue from direct time of flight measurement,'' *Phys. Med. Biol.* **33**(12), 1433–1442 (1988).
14. M. Ferrari, Q. Wei, L. Carraresi, R. A. De Blasi, and G. Zaccanti, ''Time-resolved spectroscopy of human forearm,'' *J. Photochem. Photobiol.* **16**, 141–153 (1992).
15. P. van der Zee, M. Cope, S. R. Arridge, M. Essenpreis, L. A. Potter,

A. D. Edwards, J. S. Wyatt, D. C. McCormick, S. C. Roth, E. O. R. Reynolds, and D. T. Delpy, ''Experimentally measured optical pathlengths for the adult head, calf and forearm and the head of the newborn infants as a function of inter optode spacing,'' *Adv. Exp. Med. Biol.* **316**, 143–153 (1992).
16. R. G. Steen, K. Kitagishi, and K. Morgan, ''*In vivo* measurement of tumor blood oxygenation by near-infrared spectroscopy: immediate effects of pentobarbital overdose or carmustine treatment,'' *J. Neuro-Oncol.* **22**, 209–220 (1994).
17. H. Liu, ''Unified analysis of the sensitivities of reflectance and path length to scattering variations in a diffusive medium,'' *Appl. Opt.* **40**(10), 1742–1746 (2001).
18. E. L. Hull, D. L. Conover, and T. H. Foster, ''Carbogen-induced changes in rat mammary tumour oxygenation reported by near infrared spectroscopy,'' *British J. Cancer* **79**(11/12), 1709–1716 (1999).
19. R. L. Fournier, ''Oxygen transport in biological systems,'' Chap. 4 in *Basic Transport Phenomena in Biomedical Engineering*, pp. 87–94, Taylor & Francis, Lillington (1999).
20. P. Peschke, E. W. Hahn, F. Lohr, F. Brauschweig, G. Wolber, I. Zuna, and M. Wannenmacher, ''Differential sensitivity of three sublines of the rat Dunning prostate tumor system R3327 to radiation and/or local tumor hyperthermia,'' *Radiat. Res.* **150**, 423–430 (1998).
21. E. W. Hahn, P. Peschke, R. P. Mason, E. E. Babcock, and P. P. Antich, ''Isolated tumor growth in a surgically formed skin pedicle in the rat: a new tumor model for NMR studies,'' *Magn. Reson. Imaging* **11**, 1007–1017 (1993).
22. Y. Yang, H. Liu, X. Li, and B. Chance, ''Low-cost frequency-domain photon migration instrument for tissue spectroscopy, oximetry, and imaging,'' *Opt. Eng.* **36**, 1562–1569 (1997).
23. M. H. Friedman, ''Gas transport,'' Chap. 9 in *Principles and Models of Biological Transport*, pp. 240–242, Springer, Berlin Heidelberg (1986).
24. H. Liu, A. H. Hielscher, F. K. Tittel, S. L. Jacques, and B. Chance, ''Influence of blood vessels on the measurement of hemoglobin oxygenation as determined by time-resolved reflectance spectroscopy,'' *Med. Physics* **22**, 1209–1217 (1995).
25. S. Hunjan, D. Zhao, A. Constantinescu, E. W. Hahn, P. Antich, and R. P. Mason, ''Tumor oximetry: demonstration of an enhanced dynamic mapping procedure using fluorine-19 echo planar magnetic resonance imaging in the dunning prostate R3327-AT1 rat tumor,'' *Int. J. Radiat. Oncol., Biol., Phys.* **49**, 1097–1108 (2001).
26. B. R. Barker, R. P. Mason, N. Bansal, and R. M. Peshock, ''Oxygen tension mapping by ^{19}F echo planar NMR imaging of sequestered perfluorocarbon,'' *JMRI* **4**, 595–602 (1994).
27. S. I. Fox, ''Respiratory physiology,'' Chap. 16 in *Human Physiology*, pp. 508–513, McGraw-Hill, Boston (1999).
28. G. Brix, J. Debus, M. Mueller-Schimpfle, P. Peschke, P. Huber, H. J. Zabel, and W. Lorenz, ''MR-tomographische Quantifizierung struktureller und funktioneller Gewebeveraenderungen an stosswellentherapierten Dunning-Prostata-Tumoren,'' *Z. Med. Phys.* **3**, 76–82 (1993).
29. R. P. Mason, F. M. H. Jeffrey, C. R. Malloy, E. E. Babcock, and P. P. Antich, ''A noninvasive assessment of myocardial oxygen tension: ^{19}F NMR spectroscopy of sequestered perfluorocarbon emulsion,'' *Magn. Reson. Med.* **27**, 310–317 (1992).